

Publisher: GSA  
Journal: GEOL: Geology  
DOI:10.1130/G39801.1

1 **Genesis of the world's largest rare earth element**  
2 **deposit, Bayan Obo, China: protracted mineralization**  
3 **evolution over ~1 billion years**

4 **Wenlei Song<sup>1</sup>, Cheng Xu<sup>1\*</sup>, Martin P. Smith<sup>2</sup>, Anton R. Chakhmouradian<sup>3</sup>, Marco**  
5 **Brenna<sup>4</sup>, Jindřich Kynický<sup>5</sup>, Wei Chen<sup>6</sup>, Yueheng Yang<sup>7</sup>, Miao Deng<sup>1</sup>, and Haiyan**  
6 **Tang<sup>8</sup>**

7 *<sup>1</sup>Key Laboratory of Orogenic Belts and Crustal Evolution, School of Earth and Space*  
8 *Sciences, Peking University, Beijing 100871, China*

9 *<sup>2</sup>School of Environment and Technology, University of Brighton, Brighton BN24GJ, UK*

10 *<sup>3</sup>Department of Geological Sciences, University of Manitoba, Manitoba R3T2N2,*  
11 *Canada.*

12 *<sup>4</sup>Department of Geology, University of Otago, Dunedin 9054, New Zealand*

13 *<sup>5</sup>Department of Geology and Pedology, Mendel University, Brno 361300, Czech Republic*

14 *<sup>6</sup>State Key Lab of Geological Processes and Mineral Resources, Wuhan 430074, China*  
15 *University of Geosciences, China*

16 *<sup>7</sup>Institute of Geology and Geophysics, Chinese Academy of Sciences, Beijing 100029,*  
17 *China*

18 *<sup>8</sup>College of Earth Science, Jilin University, Changchun 130012, China*

19 *\*E-mail: xucheng1999@pku.edu.cn*

20 **ABSTRACT**

21 The unique, giant, REE deposit at Bayan Obo is the world's largest REE deposit. It  
22 is geologically complex and its genesis is still debated. Here, we report in situ Th-Pb dating

23 and Nd isotope ratios for monazite and Sr isotope ratios for dolomite and apatite from fresh  
24 drill-cores. The measured monazite ages (361–913Ma) and previously reported  
25 whole-rock Sm-Nd data show a linear relationship with initial Nd isotope ratio, suggesting  
26 a single-stage evolution from a Sm-Nd source that was formed before 913Ma. All  
27 monazites show consistent  $\epsilon\text{Nd}_{(1.3\text{Ga})}$  values ( $0.3 \pm 0.6$ ) close to those of the adjacent 1.3Ga  
28 carbonatite and mafic dikes. The primary dolomite and apatite show lower  $^{87}\text{Sr}/^{86}\text{Sr}$  ratios  
29 (0.7024–0.7030) than the recrystallized dolomite (0.7038–0.7097). The REE ores at Bayan  
30 Obo are interpreted to have originally formed as products of ~1.3Ga carbonatitic  
31 magmatism and undergone subsequent thermal perturbations induced by Sr-rich, but  
32 REE-poor metamorphic fluids derived from nearby sedimentary rocks.

### 33 INTRODUCTION

34 The rare earth elements (REE) have become the focus of international attention  
35 because of their industrial importance to the development of “low carbon” energy and  
36 transportation technologies, and because the global REE market is extremely sensitive to  
37 geopolitically driven supply limitations (Hatch, 2012). The availability of REE for future  
38 markets is a growing concern in the developed world because global demand for these  
39 resources is expected to grow significantly (Verplanck and Hitzman, 2016). China, the  
40 United States, Russia, Canada, Brazil, Australia, India and Malaysia account for the  
41 majority of the world’s REE reserves. China presently contains ~40% of the global REE  
42 resources (Weng et al., 2015), concentrated primarily in the world’s largest REE deposit at  
43 Bayan Obo. This deposit has attracted inordinate attention from researchers (over 100  
44 papers in peer-reviewed journals just in the past decade) because of its unparalleled  
45 endowment in REE (>100Mt REE<sub>2</sub>O<sub>3</sub>, Weng et al., 2015). The genesis of the Bayan Obo

46 structure and its resources has been the subject of debate for over 50 years. There is no  
47 consensus concerning either the age of mineralization (~1300 to ~400Ma; Yang et al.,  
48 2017), or the number of mineralization stages (Chao, 1997). Genetic models proposed for  
49 Bayan Obo range from sedimentary deposition (Chao, 1997), to metasomatic reworking of  
50 metasedimentary marbles by carbonatitic (Smith et al., 1999) or subduction-derived fluids  
51 (Yang et al., 2017), to igneous processes related to carbonatite emplacement (Le Bas et al.,  
52 2007).

53 Monazite is one of the principal REE hosts in the Bayan Obo deposit. Here we  
54 report integrated, in situ, high-precision Th-Pb ages and Nd isotope ratios of monazite  
55 samples from an 1776 m long drill core section from the Bayan Obo deposit. The monazite  
56 data were combined with in situ apatite and dolomite isotope analyses to show that the  
57 Bayan Obo REE mineralization is of Mid-Mesoproterozoic age and of carbonatitic origin,  
58 and shows no evidence of any significant REE contribution from external sources. This  
59 Mid-Mesoproterozoic mineralization was subsequently modified by younger thermal  
60 events.

## 61 **GEOLOGY OF THE DEPOSIT AND SAMPLES**

62 The Bayan Obo deposit is located at the northern margin of the North China Craton  
63 (NCC). The basement comprises the Archean Wutai Group (gneisses and migmatites) and  
64 Proterozoic Bayan Obo Group. The latter has been subdivided into nine lithological units,  
65 conventionally referred to as H1-H9 in ascending chronological order. The Bayan Obo  
66 Group is composed predominantly of meta-sandstones and slates, except for the H8  
67 dolomite rock (Fig. DR1 in the GSA Data Repository<sup>1</sup>). Volcanic rocks of trachytic, dacitic  
68 and rhyolitic composition, as well as mafic dikes, have been found within the H9 group

69 (Zhang et al., 2003; Yang et al., 2011). The metamorphic clastic sequences of the Bayan  
70 Obo Group represent sedimentary units deposited within the Bayan Obo pericratonic rift.  
71 The REE deposit is hosted by the H8 dolomite rock, which extends for 18km laterally at a  
72 width of >1km, and occurs as a spindle-shaped stratiform body. About 100 carbonatite  
73 dikes are found adjacent to the deposit, intruding the Bayan Obo Group metasediments  
74 (Yang et al., 2011). The REE orebodies consist of disseminated, banded and massive ores,  
75 most of which are associated with dolomite, silicates (in particular, alkali clinopyroxene,  
76 amphibole and mica), apatite, fluorite and magnetite.

77         The studied drill core was extracted from the Eastern orebody, within the H8 unit,  
78 and has a total length of 1776m. Compared to the H8 unit exposed at the surface, which  
79 underwent extensive metasomatic alteration and deformation, and contains abundant  
80 aegirine, riebeckite, phlogopite and late-stage fluorite-barite veins superposed over the  
81 primary mineral assemblage, the drill samples are relatively fresh. The examined rocks are  
82 composed predominantly of fine- to coarse-grained dolomite. Most of the dolomite is  
83 euhedral to subhedral, and shows evidence of recrystallization with the development of  
84 triple grain junctions. Some of the fine-grained, anhedral dolomites occur as a matrix to the  
85 porphyritic dolomites (Fig. DR2), defining a primary, igneous texture. The studied drill  
86 core shows significant variations in total light REE<sub>2</sub>O<sub>3</sub> content, which locally reaches  
87 5.8wt.% (Fig. DR3; Table DR1; for methods, see Data Repository). Textural observations  
88 show that the early disseminated monazite was usually partially replaced and overgrown  
89 by bastnäsite and apatite (Fig. 1a). Late monazite occurs as monominerallic veinlets, or is  
90 associated with bastnäsite veinlets (Fig. 1b). Primary apatite was partially corroded and  
91 overgrown by a rim of monazite (Fig. 1c). Recrystallized apatite occurs as veinlets and

92 clusters with bastnäsite (Fig. 1d). The textural evolution of REE minerals indicates  
93 extensive metamorphic and metasomatic recrystallization (Smith et al., 1999).

## 94 **RESULTS**

95 The Th-Pb ages were combined with Nd isotopic ratio measurements done  
96 independently and in situ on the same monazite grains, to calculate the initial  
97 ( $^{143}\text{Nd}/^{144}\text{Nd}$ )<sub>i</sub> ratios at the time of formation (Tables DR2,3). These monazites show  
98 homogeneous internal textures (Fig. DR4), and have variable ages, ranging from  $361 \pm$   
99  $6\text{--}913 \pm 15\text{Ma}$ . Their corresponding  $\epsilon\text{Nd}(t)$  values fall between  $-6.9$  and  $-18$ . However, all  
100 samples show similar  $T_{\text{CHUR}}(\text{Nd})$  model ages ranging from 1.56 to 1.67Ga, implying  
101 derivation from the same source. The inferred ore-forming events at Bayan Obo have been  
102 previously constrained chronologically on the basis of whole-rock and mineral  
103 assemblages from surface samples, which show a wide range of ages with distinct  
104 frequency peaks at  $\sim 1.3\text{Ga}$  and  $\sim 400\text{Ma}$  (Yang et al., 2017). However, the REE-rich  
105 carbonatite dikes adjacent to the orebodies give a consistent Mid-Mesoproterozoic age of  
106 ca. 1.3Ga (Fig. 2). The Sm-Nd isochron ages of volcanic rocks and mafic dikes in the  
107 Bayan Obo deposit are also close to 1.3Ga. Figure 2 shows the measured monazite ages  
108 plotted versus their corresponding  $\epsilon\text{Nd}(t)$  values, and provides some of the previously  
109 reported Sm-Nd isochron ages and  $\epsilon\text{Nd}(t)$  values for reference. Notably, the new and  
110 published data show a good correlation, indicating a single-stage Nd isotopic evolution  
111 from a single source. Late-stage, magma-derived melts or fluids could serve as a source of  
112 REE, but this model would require that the later-emplaced magmas had very low Nd  
113 isotopic ratios. This is clearly not the case: all reported Neoproterozoic to Carboniferous  
114 igneous rocks in the northern NCC plot above the Nd isotopic evolution line for Bayan

115 Obo (Fig. 2). Therefore, we infer that late-stage changes in the REE mineralization defined  
116 by this evolution line were due to remobilization of these elements from the already  
117 existing orebody of Mid-Mesoproterozoic age. This interpretation is supported by textural  
118 evidence, such as metasomatic replacement of early monazite and apatite accompanied by  
119 the development of new REE minerals (Fig. 1). The trace element and isotope data  
120 described below further support the interpretation of the timing of primary REE  
121 mineralization.

122         The origin of the H8 dolomite rock hosting the deposit has been debated. The two  
123 “end-member” hypotheses are igneous crystallization from carbonatitic magma (Le Bas et  
124 al., 2007) and sedimentary deposition (Chao, 1997). Our Nd isotope evolution line is  
125 remarkably different from that characterizing typical sedimentary rocks from units H1-H3,  
126 in which the ( $^{143}\text{Nd}/^{144}\text{Nd}$ )<sub>i</sub> ratio, calculated from 1.3Ga to 400Ma, is markedly lower than  
127 in the REE minerals (Fig. 2). Both dolomite and apatite analyzed in this study show high Sr  
128 contents (Table DR4), typical of carbonatitic minerals (Hornig-Kjarsgaard, 1998).  
129 Different textural types of dolomite and apatite are characterized by distinct REE  
130 distribution patterns (Fig. 3). The primary dolomite shows relatively low REE content  
131 (La<10ppm) and a flat distribution pattern with (La/Yb)<sub>cn</sub> = 1–5. The recrystallized  
132 dolomite is characterized by a much more varied and higher REE content (La =  
133 16–109ppm) and stronger enrichment in light REE, with (La/Yb)<sub>cn</sub> = 8–32. The two  
134 generations also differ in their key REE ratios, i.e., the primary variety has higher Eu/Eu\*  
135 and Y/Ho values relative to the recrystallized dolomite. Early disseminated apatite is  
136 significantly enriched in REE (La>1400ppm) and shows a higher Eu/Eu\* but lower Y/Ho  
137 values than the paragenetically later generation confined to the veinlets (Fig. DR5).

138           The textural relations and extreme isotopic variability of the Bayan Obo monazite  
139 imply that it is a product of dissolution-precipitation processes and that its Th-Pb budget  
140 was modified over an extended period of time. The extended history of metasomatism at  
141 Bayan Obo is recorded in the monazite ages, spanning from 361 to 913Ma. The primary  
142 REE mineralization must have formed earlier than 913Ma and may have occurred ca.  
143 1.3Ga, as indicated by the Sm-Nd isochron ages of the ore-bearing H8 unit and spatially  
144 associated REE-enriched carbonatites (Fig. 2). These previously studied samples have  
145 initial Nd isotopic ratios similar to those of the monazite studied in the present work if  
146 calculated for 1.3Ga ( $\epsilon\text{Nd}_{1.3\text{Ga}} = 0.3 \pm 0.6$ ), implying a common mantle source. In situ Sr  
147 isotopic analysis of the primary dolomite and apatite also gave low  $^{87}\text{Sr}/^{86}\text{Sr}$  values (Table  
148 DR5, 0.7024–0.7030), which are far less radiogenic than typical marine carbonates and  
149 further support a non-sedimentary origin (Fig. 3). However, the late generations of  
150 recrystallized dolomite have variable and high Sr isotopic compositions (0.7038–0.7097).  
151 The present-day Sr isotopic ratios measured in the primary dolomite and apatite are  
152 considered to approximate the initial  $^{87}\text{Sr}/^{86}\text{Sr}$  values because these minerals contain high  
153 levels of Sr, but negligible Rb and thus, are characterized by very low Rb/Sr ratios. Similar  
154 initial Sr isotopes (0.7029–0.7030) have been reported from ~1.3Ga carbonatite dikes  
155 without contamination by feldspar from the wall rocks in Bayan Obo (Le Bas et al., 2007).

## 156 **DISCUSSION AND CONCLUSION**

157           A newly reported zircon age ( $1301 \pm 12\text{Ma}$ ) on REE-rich carbonatites at Bayan  
158 Obo supports the model of Mid-Mesoproterozoic primary mineralization (Zhang et al.,  
159 2017). The  $^{87}\text{Sr}/^{86}\text{Sr}$  ratios of primary dolomite and apatite are close to the Bulk Earth  
160 value (0.7029) at 1.3Ga. The  $\epsilon\text{Nd}_{1.3\text{Ga}}$  value of monazite is also close to the Chondritic

161 Uniform Reservoir value, implying that the ore-bearing dolomite rock may be derived  
162 from a primary, non-depleted mantle source, perhaps residing within the less-accessible  
163 parts of the mantle, or in the depleted lithospheric mantle modified by old subducted  
164 materials. Experiments show that primary carbonatitic melts derived from carbonated  
165 peridotites contain relatively low REE abundances (Foley et al., 2009) and must  
166 consequently undergo extensive fractionation in the crust to produce the level of REE  
167 enrichment. Initially low REE concentrations in carbonatitic magmas are typically  
168 dispersed among such major rock-forming constituents as calcite and apatite  
169 (Hornig-Kjarsgaard, 1998), preventing the development of REE mineralization. In  
170 contrast, primary carbonatitic magmas can be derived by partial melting of carbonated  
171 eclogites (Thomson et al., 2016). In the Trans-North China Orogen of the NCC (i.e.,  
172 ~300km southeast of Bayan Obo), several occurrences of Paleoproterozoic carbonatite  
173 dikes were found to contain high-pressure eclogite xenoliths of recycled crustal origin (Xu  
174 et al., 2017a). This discovery provides unambiguous evidence that subducted material is  
175 present in the mantle beneath the northern NCC. Seismic imaging of the NCC across the  
176 Trans-North China Orogen (Zheng et al., 2009) provides strong support to  
177 Paleoproterozoic (1.9–2.1Ga) westward subduction beneath the Western Block of the  
178 Craton at the time when it is inferred to have been part of the Columbia supercontinent.  
179 Numerous diabase dikes emplaced in the northern NCC (Fig. DR1) are considered to be  
180 related to the Mid-Mesoproterozoic breakup of Columbia (see Zhang et al., 2017). The  
181 mafic dikes in the northern NCC share geochemical characteristics of both ocean-island  
182 basalts and island-arc volcanic rocks, as can be seen in tectonic-setting-based  
183 discrimination diagrams (Fig. DR6). Geochemically, these dikes resemble basaltic



184 magmatism whose mantle source was influenced by previous subduction events, and are  
185 distinctly different from purely intraplate volcanic rocks in the NCC. In particular, the  
186 Bayan Obo mafic dikes and volcanic rocks in unit H9 show consistent negative Nb, Ta and  
187 Ti anomalies (normalized to the primary mantle values), and are compositionally similar to  
188 arc basalts (Fig. DR7). Crustal contamination as a source of these geochemical deviations  
189 can be ruled out because the mafic dikes in the northern NCC show a consistent Nd  
190 isotopic signature ( $\epsilon\text{Nd}_{1.3\text{Ga}} = -0.5\text{--}1.9$ ; Yang et al., 2011). Therefore, we consider that  
191 subduction modification pre-conditioned the mantle source to generate the Bayan Obo  
192 carbonatite REE deposit.

193 Our mineralogical and geochemical results suggest that the primary REE  
194 mineralization at Bayan Obo was modified by externally derived fluids, which involved  
195 the development of superimposed mineralization and recrystallization of the primary  
196 minerals. The metasomatic fluids contain a crustal component, as indicated by a negative  
197 shift in  $\text{Eu}/\text{Eu}^*$  value and higher  $^{87}\text{Sr}/^{86}\text{Sr}$  ratios in the recrystallized dolomite and apatite  
198 (Fig. 3, Fig. DR5). The Y/Ho trends exhibited by dolomite and apatite are mutually  
199 complementary, indicating structural controls over Y versus Ho partitioning between  
200 crystals and the fluids, whereas both minerals show depletion in Eu with recrystallization.  
201 The C-O isotope data from the deposit also show a large variation and plot between mantle  
202 and sediment fields (Yang et al., 2017). Moreover, the fluids must have been poor in REE,  
203 but rich in Sr to explain the positive  $^{87}\text{Sr}/^{86}\text{Sr}$  excursion. Caledonian subducted  
204 slab-derived fluids, as proposed by Yang et al. (2017), are unlikely to be responsible for the  
205 observed geochemical trends, because such fluids would be expected to have radiogenic  
206 Nd isotopes (Xu et al., 2017b). Their interaction with the H8 unit would inevitably modify

207 its Nd isotopic signature, causing deviation of monazite  $\epsilon\text{Nd}(t)$  values from the continuous  
208 evolutionary line shown in Figure 2. Moreover, the Neoproterozoic to Carboniferous  
209 magmatism in the northern NCC could not provide fluids sufficiently depleted in  
210 radiogenic Nd to explain the low negative  $\epsilon\text{Nd}(t)$  values of young Bayan Obo monazite  
211 generations. The sedimentary rocks present in the sequence at Bayan Obo are a viable  
212 alternative source of metasomatizing fluids. These rocks show elevated Sr levels (up to  
213 580ppm) coupled with a strongly radiogenic Sr isotopic signature  
214 ( $^{87}\text{Sr}/^{86}\text{Sr}_{(985\text{Ma})}=0.7147$ ), but are poor in REE (Zhang et al., 2003), and may have  
215 contributed this signature to the post-ore metasomatic fluids involved in dolomite and  
216 apatite recrystallization. These sedimentary rocks underwent metamorphism to various  
217 degrees (from greenschist to low amphibolites facies conditions) and could serve as a  
218 persistent fluid source responsible for textural and geochemical changes in the H8  
219 dolomite rock.

220 In conclusion, our interpretation of the isotopic and trace element characteristics of  
221 monazite, dolomite and apatite support the derivation of primary REE from a  
222 Mid-Mesoproterozoic carbonatitic source. The apparent discrepancy in the behavior of Sr  
223 and Nd isotopes highlights the importance of multi-systemic approach to geologically  
224 complex mineral deposits, and reflects a protracted history of metasomatism induced by  
225 Sr-rich, REE-poor fluids. In a similar case, the Nolans Bore REE deposit in Australia has  
226 been found to have experienced multiple episodes of recrystallization/internal reworking  
227 over a period of at least 1 billion years after primary ore formation (Schoneveld et al.,  
228 2015). The resetting of the ore system may be common in most REE deposits, and may be  
229 critical in the high grade of some deposits. Interpreting geochronological results from the

230 REE orebodies should be undertaken with caution. However, with the utilization of  
231 petrographic constrained analyses, recrystallization processes may be related to regional  
232 tectonic events, and therefore complex REE orebodies could be used to unravel their  
233 tectonic evolution.

#### 234 **ACKNOWLEDGMENTS**

235 This research was financially supported by Chinese NSF (41573033; 41688103;  
236 41773022). We are particularly grateful to Carl Spandler, Philip L Verplanck and Franco  
237 Pirajno for their constructive comments, and J. Brendan Murphy for handling our paper.

#### 238 **REFERENCES CITED**

- 239 Chao, E.C.T., 1997, The sedimentary carbonate-hosted giant Bayan Obo REE-Fe-Nb ore  
240 deposit of Inner Mongolia, China: A corner stone example for giant polymetallic ore  
241 deposits of hydrothermal origin: U.S. Geological Survey Bulletin, v. 2143, p. 1–65.
- 242 Foley, S.F., Yaxley, G.M., Rosenthal, A., Buhre, S., Kiseeva, E.S., Rapp, R.P., and Jacob,  
243 D.E., 2009, The composition of near-solidus melts of peridotite in the presence of CO<sub>2</sub>  
244 and H<sub>2</sub>O between 40 and 60 kbar: *Lithos*, v. 112, p. 274–283,  
245 <https://doi.org/10.1016/j.lithos.2009.03.020>.
- 246 Hatch, G.P., 2012, Dynamics in the global market for rare earths: *Elements*, v. 8,  
247 p. 341–346, <https://doi.org/10.2113/gselements.8.5.341>.
- 248 Hornig-Kjarsgaard, I., 1998, Rare earth elements in sovitic carbonatites and their mineral  
249 phases: *Journal of Petrology*, v. 39, p. 2105–2121,  
250 <https://doi.org/10.1093/petrology/39.11.2105>.
- 251 Le Bas, M.J., Yang, X.M., Taylor, R.N., Spiro, B., Milton, J.A., and Zhang, P.S., 2007,  
252 New evidence from a calcite-dolomite carbonatite dike for the magmatic origin of the

- 253 massive Bayan Obo ore-bearing dolomite marble, Inner Mongolia, China: *Mineralogy*  
254 and *Petrology*, v. 90, p. 223–248, <https://doi.org/10.1007/s00710-006-0177-x>.
- 255 Schoneveld, L., Spandler, C., and Hussey, K., 2015, Genesis of the central zone of the  
256 Nolans Bore rare earth element deposit, Northern Territory, Australia: *Contributions*  
257 to *Mineralogy and Petrology*, v. 170, p. 11,  
258 <https://doi.org/10.1007/s00410-015-1168-x>.
- 259 Shao, J.A., Hong, D.W., and Zhang, L.Q., 2002, Genesis of Sr-Nd isotopic characteristics  
260 of igneous rocks in Inner Mongolia: *Geological Bulletin of China*, v. 21, p. 817–822.
- 261 Smith, M.P., Henderson, P., and Zhang, P., 1999, Reaction relationships in the Bayan Obo  
262 Fe-REE-Nb deposit, Inner Mongolia, China: Implications for the relative stability of  
263 rare-earth element phosphates and fluorocarbonates: *Contributions to Mineralogy and*  
264 *Petrology*, v. 134, p. 294–310, <https://doi.org/10.1007/s004100050485>.
- 265 Thomson, A.R., Walter, M.J., Kohn, S.C., and Brooker, R.A., 2016, Slab melting as a  
266 barrier to deep carbon subduction: *Nature*, v. 529, p. 76–79,  
267 <https://doi.org/10.1038/nature16174>.
- 268 Verplanck, P.L., and Hitzman, M.W., 2016, Introduction: Rare earth and critical elements  
269 in ore deposits: *Economic Geology and the Bulletin of the Society of Economic*  
270 *Geologists*, v. 18, p. 1–4.
- 271 Weng, Z., Jowitt, S.M., Mudd, G.M., and Haque, N., 2015, A detailed assessment of global  
272 rare earth element resources: Opportunities and challenges: *Economic Geology and*  
273 *the Bulletin of the Society of Economic Geologists*, v. 110, p. 1925–1952,  
274 <https://doi.org/10.2113/econgeo.110.8.1925>.

- 275 Xu, C., Kynicky, J., Smith, M.P., Kopriva, A., Brtnicky, M., Urubek, T., Yang, Y.H.,  
276 Zhao, Z., He, C., and Song, W., 2017b, Origin of heavy rare earth mineralization in  
277 South China: *Nature Communications*, v. 8, p. 14598,  
278 <https://doi.org/10.1038/ncomms14598>.
- 279 Xu, C., Kynicky, J., Tao, R.B., Liu, X., Zhang, L.F., Pohanka, M., Song, W.L., and Fei,  
280 Y.W., 2017a, Recovery of an oxidized majorite inclusion from Earth's deep  
281 asthenosphere: *Science Advances*, v. 3, p. e1601589,  
282 <https://doi.org/10.1126/sciadv.1601589>.
- 283 Yang, K.F., Fan, H.R., Santosh, M., Hu, F.F., and Wang, K.Y., 2011, Mesoproterozoic  
284 mafic and carbonatitic dikes from the northern margin of the North China Craton:  
285 Implications for the final breakup of Columbia supercontinent: *Tectonophysics*,  
286 v. 498, p. 1–10, <https://doi.org/10.1016/j.tecto.2010.11.015>.
- 287 Yang, X., Lai, X., Pirajno, F., Liu, Y., Ling, M., and Sun, W., 2017, Genesis of the Bayan  
288 Obo Fe-REE-Nb formation in Inner Mongolia, North China Craton: A perspective  
289 review: *Precambrian Research*, v. 288, p. 39–71,  
290 <http://doi.org/10.1016/j.precamres.2016.11.008>.
- 291 Zhang, S.H., Zhao, Y., and Liu, Y., 2017, A precise zircon Th-Pb age of carbonatite sills  
292 from the world's largest Bayan Obo deposit: Implications for timing and genesis of  
293 REE-Nb mineralization: *Precambrian Research*, v. 291, p. 202–219,  
294 <http://dx.doi.org/10.1016/j.precamres.2017.01.024>.
- 295 Zhang, Z.Q., Yuan, Z.X., Tang, S.H., Bai, G., and Wang, J.H., 2003, Age and  
296 Geochemistry of the Bayan Obo Ore Deposit: Beijing, Geological Publishing House,  
297 222 p.

298 Zheng, T., Zhao, L., and Zhu, R., 2009, New evidence from seismic imaging for  
299 subduction during assembly of the North China craton: *Geology*, v. 37, p. 395–398,  
300 <https://doi.org/10.1130/G25600A.1>.

301 Zhu, X.K., Sun, J., and Pan, C., 2015, Sm-Nd isotopic constraints on rare-earth  
302 mineralization in the Bayan Obo ore deposit, Inner Mongolia, China: *Ore Geology  
303 Reviews*, v. 64, p. 543–553, <https://doi.org/10.1016/j.oregeorev.2014.05.015>.

304

### 305 **FIGURE CAPTIONS**

306

307 Figure 1. Back-scattered-electron images showing the characteristic mineral assemblages  
308 and textures observed in the Bayan Obo drill core. Dol, dolomite; Mnz, monazite; Ap,  
309 apatite; Bas, bastnäsite; Mag, magnetite.

310

311 Figure 2. Trend of Nd isotopic evolution of Bayan Obo monazite with age compared to  
312 other relevant isotopic data. The dashed line is the trend line of the monazite and can be  
313 extended to 1.3Ga, where the  $\epsilon\text{Nd}(t)$  value is close to zero and similar to the  $\epsilon\text{Nd}(t)$  values  
314 of the H8 unit (Zhang et al., 2003; Zhu et al., 2015; Yang et al., 2017), mafic dikes (Yang  
315 et al., 2011) and volcanic rocks (Zhang et al., 2003) within the H9 unit, and carbonatite  
316 dikes adjacent to the deposit (Zhang et al., 2003; Le Bas et al., 2007; Yang et al., 2011).  
317 Data for sedimentary rocks (Zhang et al., 2003) from Bayan Obo and igneous rocks (Shao  
318 et al., 2002) from the northern NCC are plotted.

319

320 Figure 3. Chondrite-normalized REE patterns and  $^{87}\text{Sr}/^{86}\text{Sr}$  ratios of dolomite and apatite  
321 from the drill core. Average REE abundances were used with error bars of one standard  
322 deviation.

323

324 <sup>1</sup>GSA Data Repository item 2018xxx, methods, figures, and tables, is available online at  
325 <http://www.geosociety.org/datarepository/2018/> or on request from  
326 [editing@geosociety.org](mailto:editing@geosociety.org).

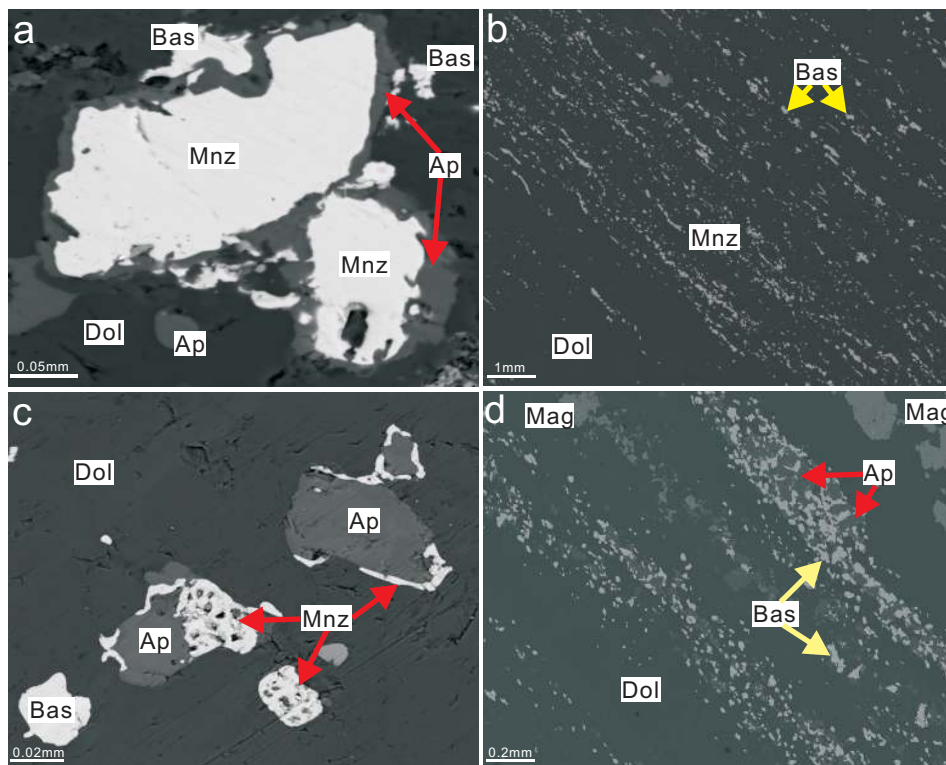


Figure 1



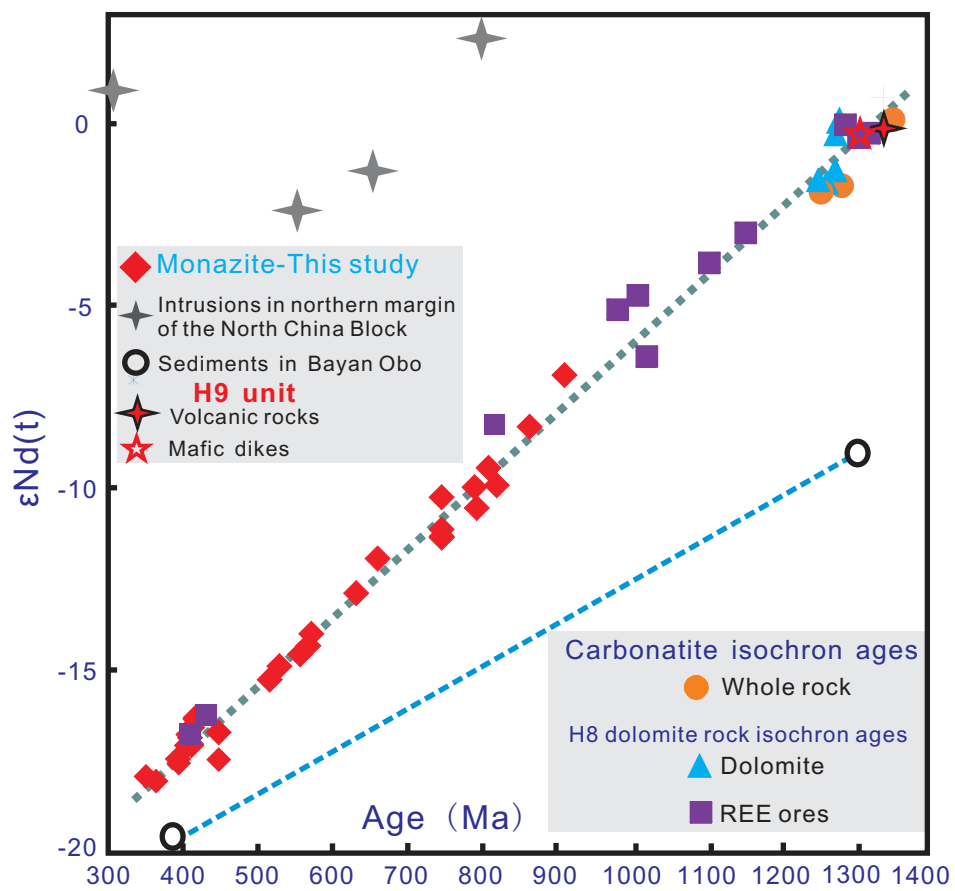


Figure 2

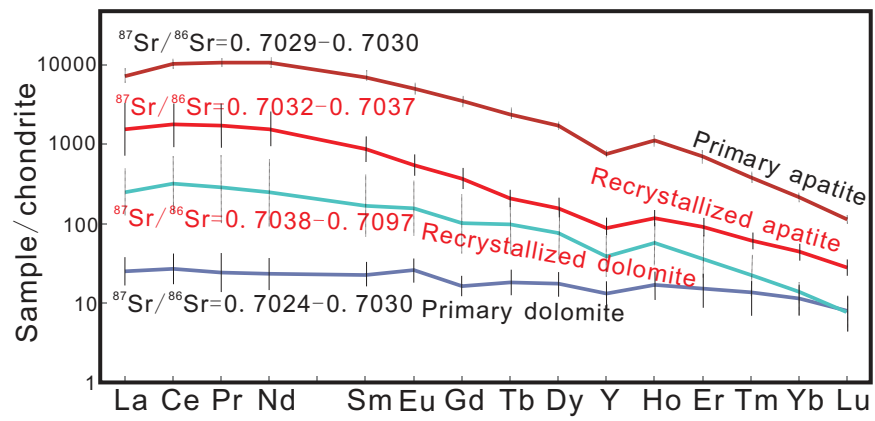


Figure 3

1 GSA Data Repository 2018XXX

2 W. Song, C. Xu<sup>\*</sup>, M.P. Smith, A.R. Chakhmouradian, M. Brenna, J. Kynický, W.  
3 Chen, Y. Yang, M. Deng, and H. Tang, 2018, Genesis of the world's largest  
4 rare earth element deposit, Bayan Obo, China: protracted mineralization  
5 evolution over ~1 billion years: *Geology*

6

## 7 **Analytical Methods**

### 8 **Whole-rock analysis**

9 Major and rare earth element abundances in drill core samples were  
10 determined by a Spectro Blue Sop inductively coupled plasma optical emission  
11 spectrometer (ICP-OES) at the School of Earth and Space Sciences, Peking  
12 University. The analytical precision is  $\pm 5\%$  for all the elements.

13

### 14 **Element mapping**

15 Compositional X-ray maps of monazites were obtained with an Oxford  
16 INCA X-MAX50 250+, energy dispersive X-ray spectrometer installed on a FEI  
17 Quanta-650FEG scanning electron microscope, at the School of Earth and  
18 Space Sciences, Peking University. The backscattered electron and  
19 energy-dispersive X-ray data acquired from the samples were combined and  
20 processed automatically to generate the most sensitive X-ray mapping. The  
21 sample, coated with a conductive Cr layer (10 nm thickness) to prevent sample  
22 charging, was analyzed in a high-vacuum mode at standard operating

1 conditions (accelerating voltage of 20 kV, probe current 5 nA).

2

### 3 **Monazite dating**

4 Monazite grains ranging from 50 to 100  $\mu\text{m}$  across were collected from the  
5 drill core using conventional heavy liquid separation techniques.  
6 Back-scattered electron images show that the crystals are compositionally  
7 homogeneous and free of inclusions. The Th-Pb dating of monazite was  
8 performed using a Cameca IMS-1280 secondary-ion mass-spectrometer  
9 (SIMS) at the Institute of Geology and Geophysics (IGG), Chinese Academy of  
10 Sciences (CAS). During the analysis, an  $\text{O}^{2-}$  primary ion beam was  
11 accelerated at 13 kV with an intensity of ca. 2-3 nA. Aperture illumination mode  
12 (Kohler illumination) was used with a 200- $\mu\text{m}$  primary beam mass filter  
13 aperture to produce even sputtering over the entire analyzed area. The  
14 ellipsoidal spot was about 20  $\times$  30  $\mu\text{m}$  in size. Positive secondary ions were  
15 extracted with a 10 kV potential. Monazite 44069 was used as a standard. A  
16  $^{207}\text{Pb}$ -based common Pb correction method was used. Further instrumental  
17 and analytical details can be found in Li et al. (2013).

18

### 19 **Trace element analysis**

20 In-situ laser-ablation analyses of dolomite and apatite in thin sections were  
21 performed by inductively-coupled-plasma mass-spectrometry (ICP-MS) at the  
22 School of Earth and Space Sciences, Peking University, using a COMPexPro

1 102 excimer laser and an Agilent7500ce/cs mass-spectrometer. The diameter  
2 of an ablation spot was 32  $\mu\text{m}$ . The NIST 610 glass was used as a calibration  
3 standard, and the Ca content measured by electron-microprobe analysis, as  
4 an internal standard. Signal intensity for indicative trace elements was  
5 monitored online during the analysis to ensure that the ablation spot was  
6 confined to the area of interest and did not sample other mineral phases or  
7 inclusions. The analytical error was estimated to be better than 5% at the ppm  
8 level.

9

#### 10 **Nd-Sr isotopic analysis**

11 The Nd isotopic composition of monazite was measured in situ by  
12 multi-collector ICP-MS using a Thermo-Finnigan Neptune instrument coupled  
13 to a 193-nm ArF excimer laser-ablation system at the IGG, CAS. The diameter  
14 of a laser spot and frequency were adjusted to between 10-24  $\mu\text{m}$  and 4-10 Hz,  
15 respectively, depending on the Nd concentration in the sample. Each spot  
16 analysis consisted of approximately 60 s of signal acquisition. More detailed  
17 information on the in-situ Nd isotopic analysis employed in the present work is  
18 available in Yang et al. (2008). The Sr isotopic compositions of dolomite and  
19 apatite were measured in situ by laser-ablation multicollector ICP-MS  
20 (Resonics + Nu instruments) at the State Key Laboratory of Geological  
21 Processes and Mineral Resources, China University of Geosciences (Wuhan).  
22 The isotopic ratios were quantified in a static multicollector mode at low

1 resolution, using seven Faraday collectors and a mass configuration array  
2 from  $^{82}\text{Kr}$  to  $^{88}\text{Sr}$  to monitor variations in Kr, Rb and Sr signals. The detailed  
3 analytical procedure and data-reduction strategy are described in Tong et al.  
4 (2015).

5

## 6 **Figure captions for Data Repository**

7 Figure DR1. Geological sketch map of the Bayan Obo deposit. a: The  
8 locations of Bayan Obo and ~1.3 Ga mafic dikes in the northern North China  
9 Craton (NCC; Yang et al., 2011; Zhang et al., 2012; Wang et al., 2014); b: The  
10 locations of drill core, carbonatite and mafic dikes in Bayan Obo.

11 Figure DR2. Drill core samples and their photomicrographs. a, b: Drill cores  
12 collected from the Eastern Orebody at a depth of 1776 m. c: Photomicrograph  
13 of dolomite (Dol) showing re-crystallization texture with the development of  
14 elongation and preferred orientation, and triple junctions between crystals.  
15 Rare earth minerals (REM) of monazite and REE-fluorocarbonates occur as  
16 veinlets. d: Photomicrograph of primary fine-grained dolomite as a matrix to  
17 porphyritic dolomite. Disseminated REM is associated with fluorite (Fl).

18 Figure DR3. Plot showing the total light REE<sub>2</sub>O<sub>3</sub> contents (La-Sm) of the drill  
19 core samples with vertical depth.

20 Figure DR4. X-ray compositional maps of representative monazite grains.

21 Figure DR5. Compositional variation of primary and recrystallized dolomite  
22 (Dol) and apatite (Ap) from the Bayan Obo drill cores. a: La/Yb<sub>cn</sub> (cn -

1 chondrite normalized) vs. total REE; b: Y/Ho vs.  $Eu/Eu^*$  (Eu anomaly).

2 Figure DR6. Revised tectonic discrimination diagrams for mafic dikes from the  
3 northern NCC. Data of the Wulahada and Wudalianchi volcanic fields in NCC  
4 are plotted as reference for cases of basaltic magmatism with the source  
5 influenced by previous subduction events (Wulahada at 142 Ma; Zhang et al.,  
6 2003) and for purely intraplate (OIB-like) volcanism from an enriched source  
7 (Wudalianchi at 10 Ma to recent; Zhang et al., 1995). The  
8 Mid-Mesoproterozoic mafic dikes (Zhang et al., 2012; Wang et al., 2014) in  
9 northern NCC plot in both IAB and OIB, and Bayan Obo data (Wang et al.,  
10 2003; Yang et al., 2011) mostly in the IAB field, indicating influence of  
11 subduction derived fluids in their mantle source. The tectonic discrimination  
12 diagrams are from Vermeesch (2006). OIB, Ocean Island Basalt; IAB, Island  
13 Arc Basalt; MORB, Middle Ocean Ridge Basalt.

14 Figure DR7. Primitive mantle normalized diagram for mafic dikes from the  
15 northern NCC. Data of OIB is from Sun and McDonough (1989), IAB based on  
16 average compositions reported by Jakes and Gill (1970), McCulloch and  
17 Gamble, (1991), and with dashed Ta abundance based on the Nb/Ta ratios  
18 reported by Stolz et al. (1996). Additional data sources are same as Fig. DR6.  
19 Note that the Bayan Obo mafic rocks have Nb, Ta and Ti negative anomalies  
20 and Pb and Sr positive anomalies resembling IAB, and have mostly lower  
21 elemental abundances than OIB, suggesting a subduction influence in their  
22 genesis.

1

## 2 **References for Data Repository**

3 Jakes, P., and Gill, J., 1970, Rare earth elements and the island arc tholeiitic  
4 series: *Earth and Planetary Science Letters*, v. 9, p. 17-28.

5 Li, Q.L., Li, X.H., Lan, Z.W., Guo, C.L., Yang, Y.N., Liu, Y., and Tang, G.Q.,  
6 2013, Monazite and xenotime U-Th-Pb geochronology by ion microprobe:  
7 dating highly fractionated granites at Xihuashan tungsten mine, SE  
8 China: *Contributions to Mineralogy and Petrology*, v. 166, p. 65-80.

9 McCulloch, M.T., and Gamble, J., 1991, Geochemical and geodynamical  
10 constraints on subduction zone magmatism: *Earth and Planetary Science*  
11 *Letters*, v. 102, p. 358-374.

12 Stolz, A., Jochum, K., Spettel, B., and Hofmann, A., 1996, Fluid-and  
13 melt-related enrichment in the subarc mantle: evidence from Nb/Ta  
14 variations in island-arc basalts: *Geology*, v. 24, p. 587-590.

15 Sun, S.-S., and McDonough, W.F., 1989, Chemical and isotopic systematics of  
16 oceanic basalts: implications for mantle composition and processes:  
17 *Geological Society, London, Special Publications* 42, p. 313-345.

18 Tong, X.R., Liu, Y., Hu, Z., Chen, H., Zhou, L., Hu, Q., Xu, R., Deng, L., Chen,  
19 C., and Gao, S., 2015, Accurate Determination of Sr Isotopic  
20 Compositions in Clinopyroxene and Silicate Glasses by  
21 LA-MC-ICP-MS: *Geostandards and Geoanalytical Research*, v. 40, p.  
22 85-89.



- 1 Vermeesch, P., 2006, Tectonic discrimination diagrams revisited:  
2 Geochemistry Geophysics Geosystems, v. 7, p. Q06017.
- 3 Wang, Q.H., Yang, H., Yang, D.B., and Xu, W.L., 2014, Mid-Mesoproterozoic  
4 (~ 1.32 Ga) diabase swarms from the western Liaoning region in the  
5 northern margin of the North China Craton: Baddeleyite Pb–Pb  
6 geochronology, geochemistry and implications for the final breakup of the  
7 Columbia supercontinent: Precambrian Research, v. 254, p. 114-128.
- 8 Wang, Y., Qiu, Y., Gao, J., and Zhang, Q., 2003, Proterozoic anorogenic  
9 magmatic rocks and their constraints on mineralizations in the Bayan Obo  
10 deposit region, Inner Mongolia: Science in China (D), v. 46, p. 26-40.
- 11 Yang, K.F., Fan, H.R., Santosh, M., Hu, F.F., and Wang, K.Y., 2011,  
12 Mesoproterozoic mafic and carbonatitic dykes from the northern margin of  
13 the North China Craton: implications for the final breakup of Columbia  
14 supercontinent: Tectonophysics, v. 498, p. 1-10.
- 15 Yang, Y.H., Sun, J.F., Xie, L.W., Fan, H.R., and Wu, F.Y., 2008, In situ Nd  
16 isotopic measurement of natural geological materials by LA-MC-ICPMS:  
17 Chinese Science Bulletin, v. 53, p. 1062-1070.
- 18 Zhang, H.F., Sun, M., Zhou, X.H., Zhou, M.F., Fan, W.M., and Zhang, J.P.,  
19 2003, Secular evolution of the lithosphere beneath the eastern North  
20 China Craton: evidence from Mesozoic basalts and high-Mg andesites:  
21 Geochimica et Cosmochimica Acta, v. 67, p. 4373-4387.
- 22 Zhang, M., Suddaby, P., Thompson, R.N., Thirlwall, M.F., and Menzies, M.A.,

1 1995, Potassic volcanic rocks in NE China: geochemical constraints on  
2 mantle source and magma genesis: *Journal of Petrology*, v. 36, p.  
3 1275-1303.

4 Zhang, S.H., Zhao, Y., and Santosh, M., 2012, Mid-Mesoproterozoic bimodal  
5 magmatic rocks in the northern North China Craton: implications for  
6 magmatism related to breakup of the Columbia supercontinent:  
7 *Precambrian Research*, v. 222-223, p. 339-367.

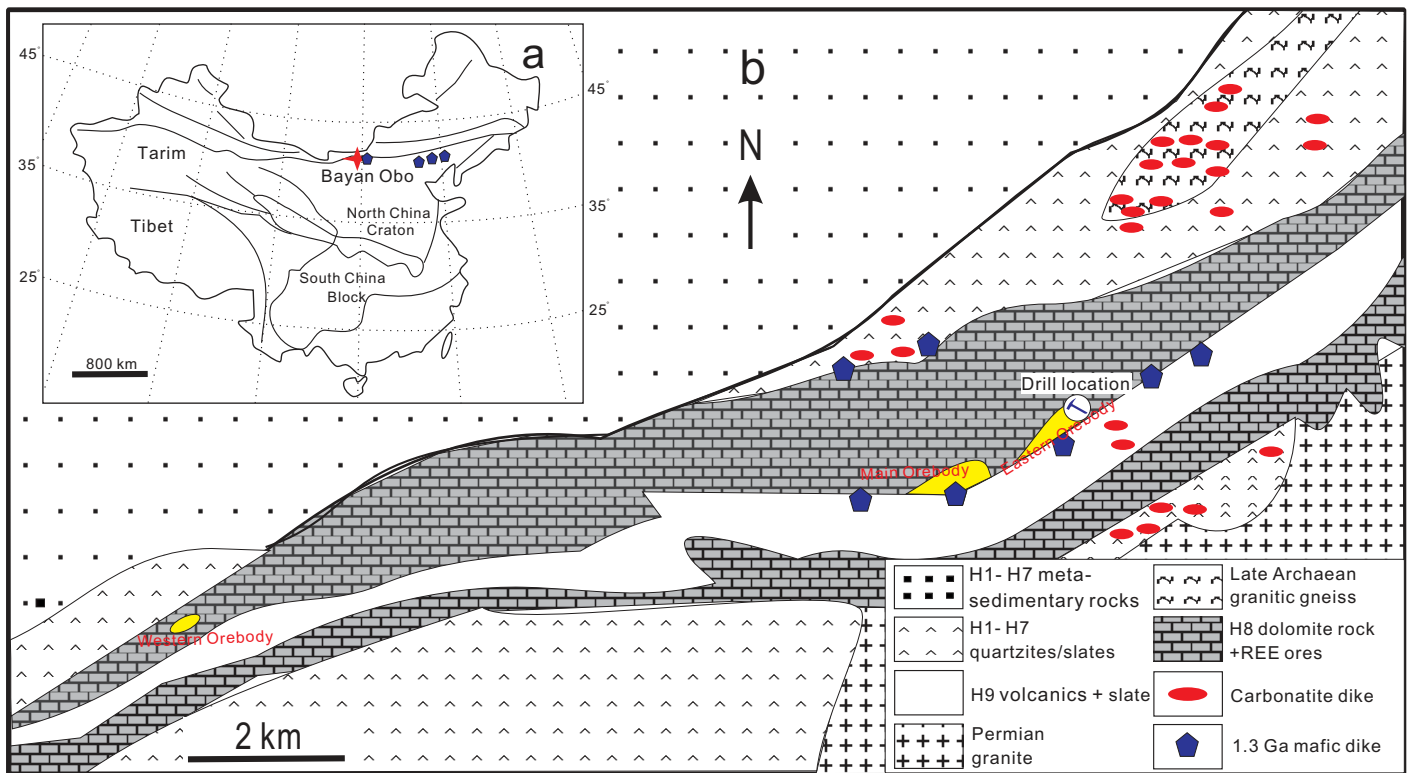


Figure DR1

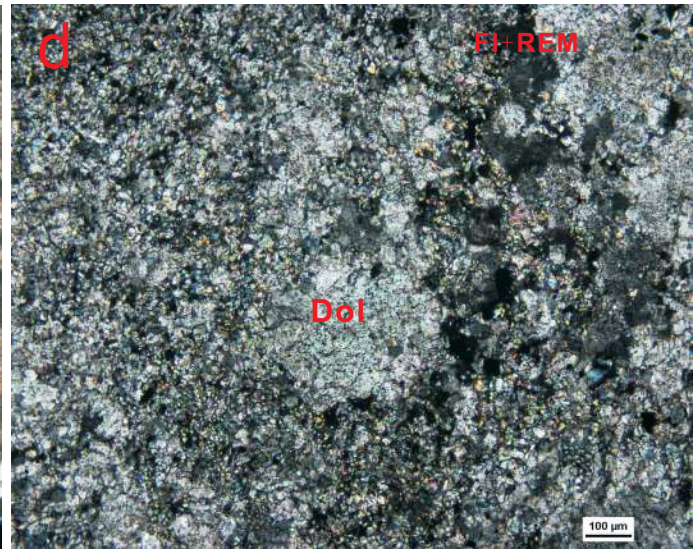
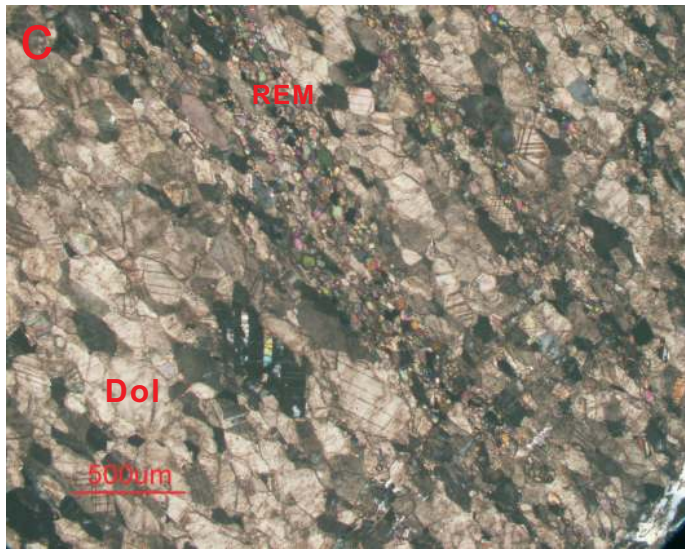
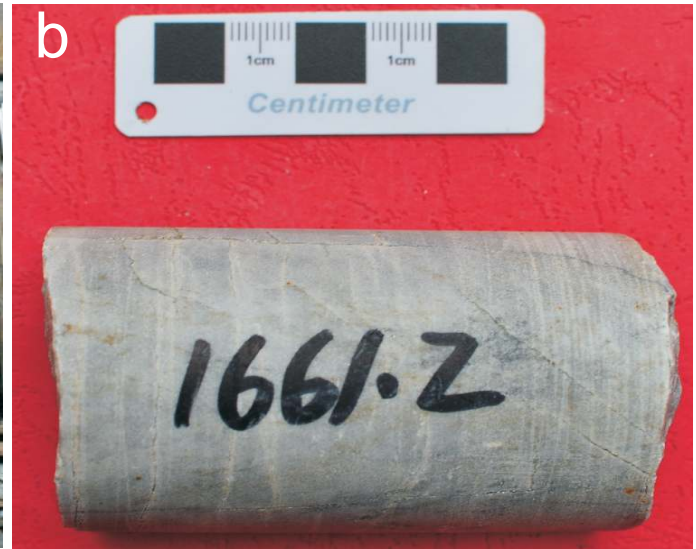


Figure DR2

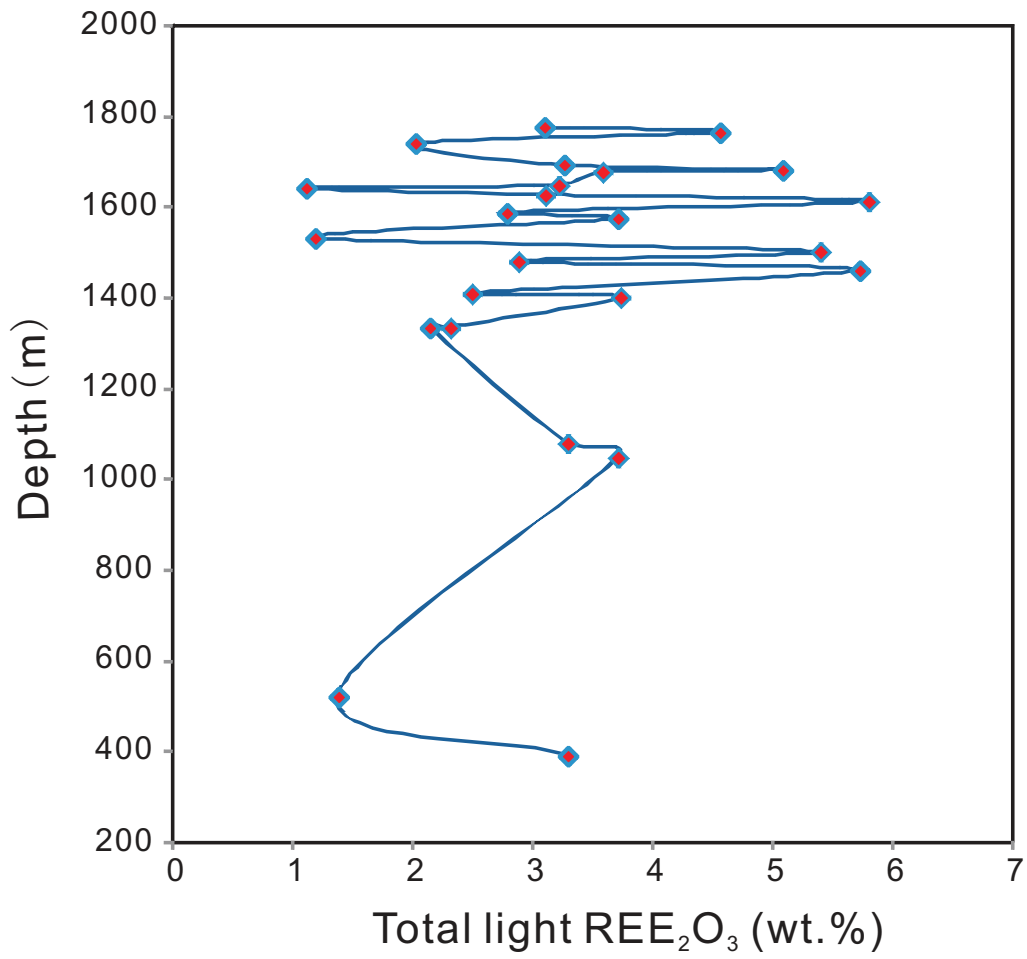


Figure DR3

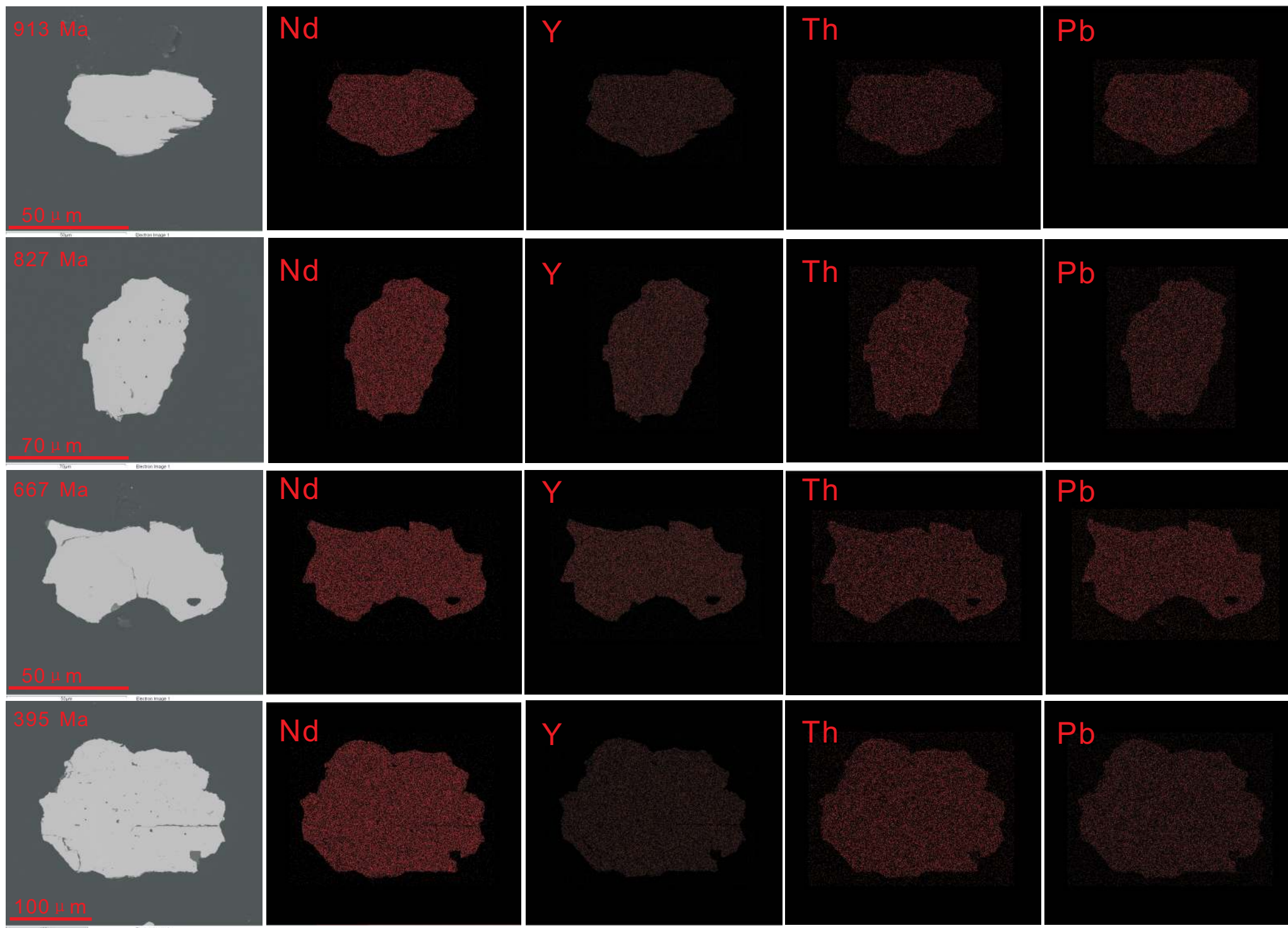


Figure DR4

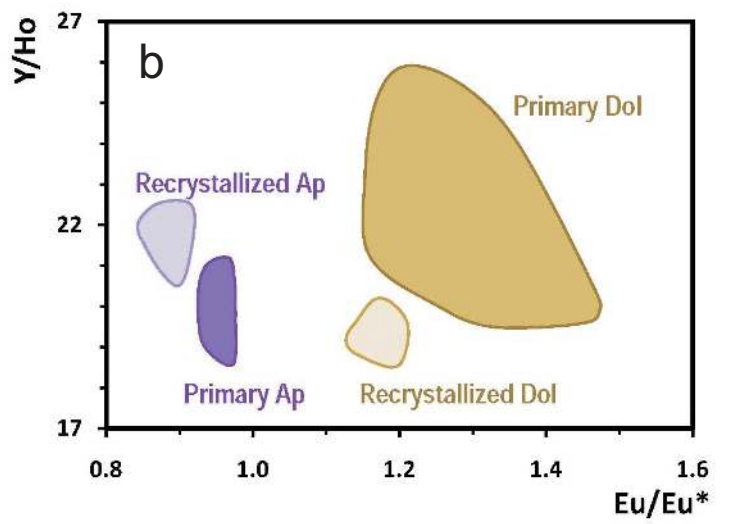
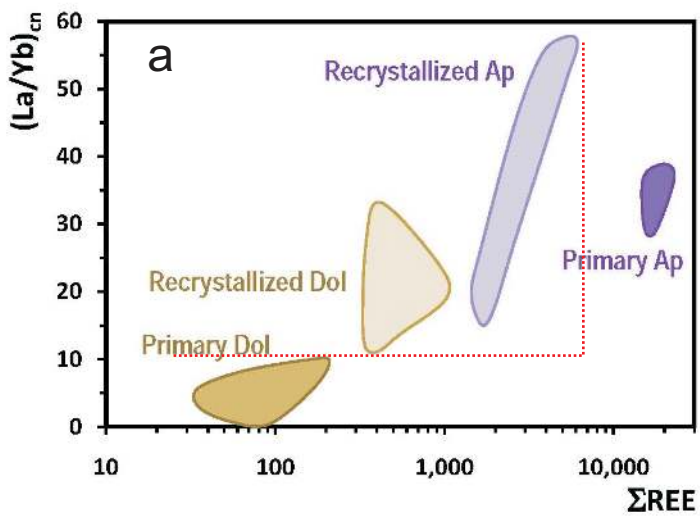


Figure DR5

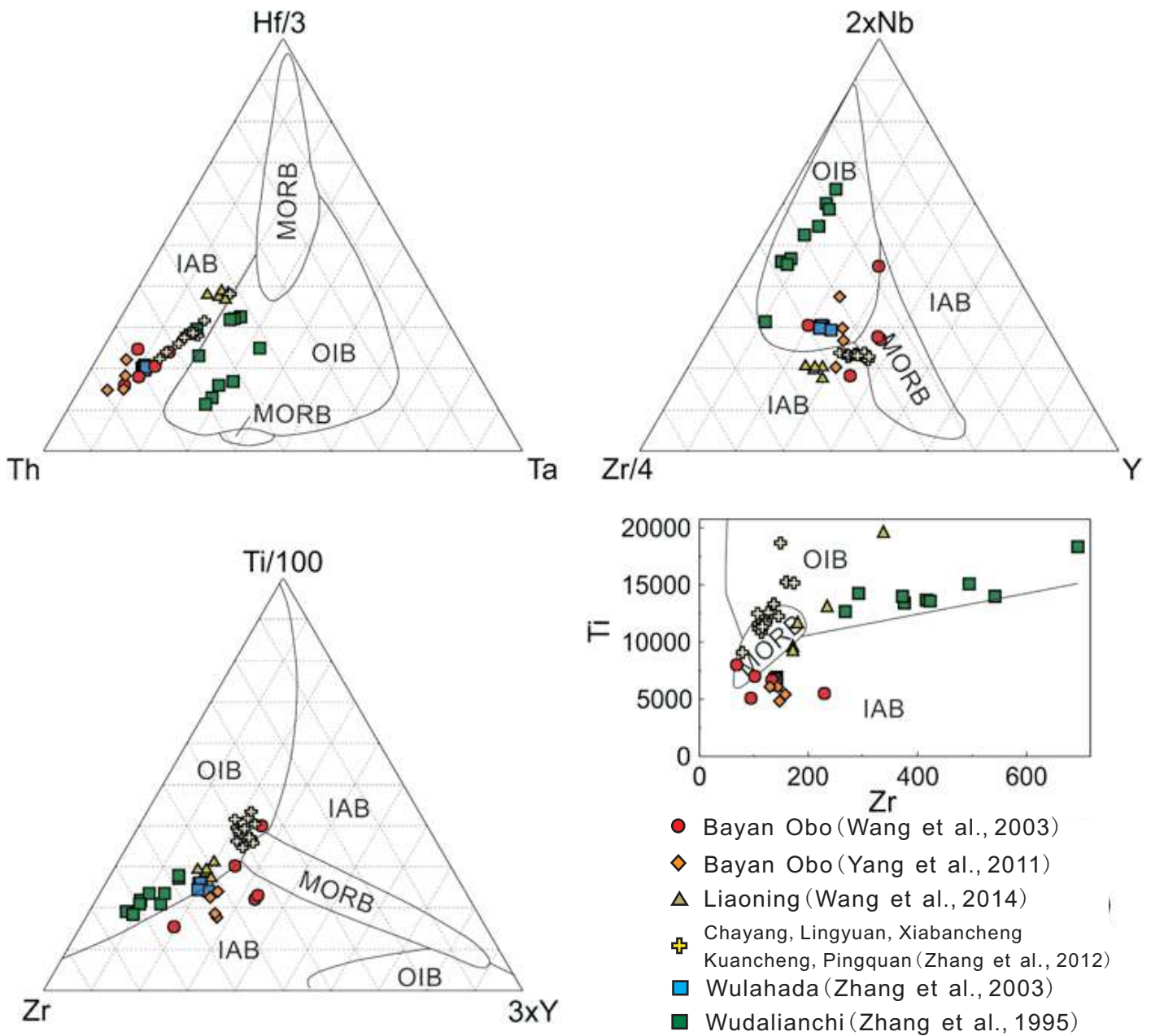


Figure DR6



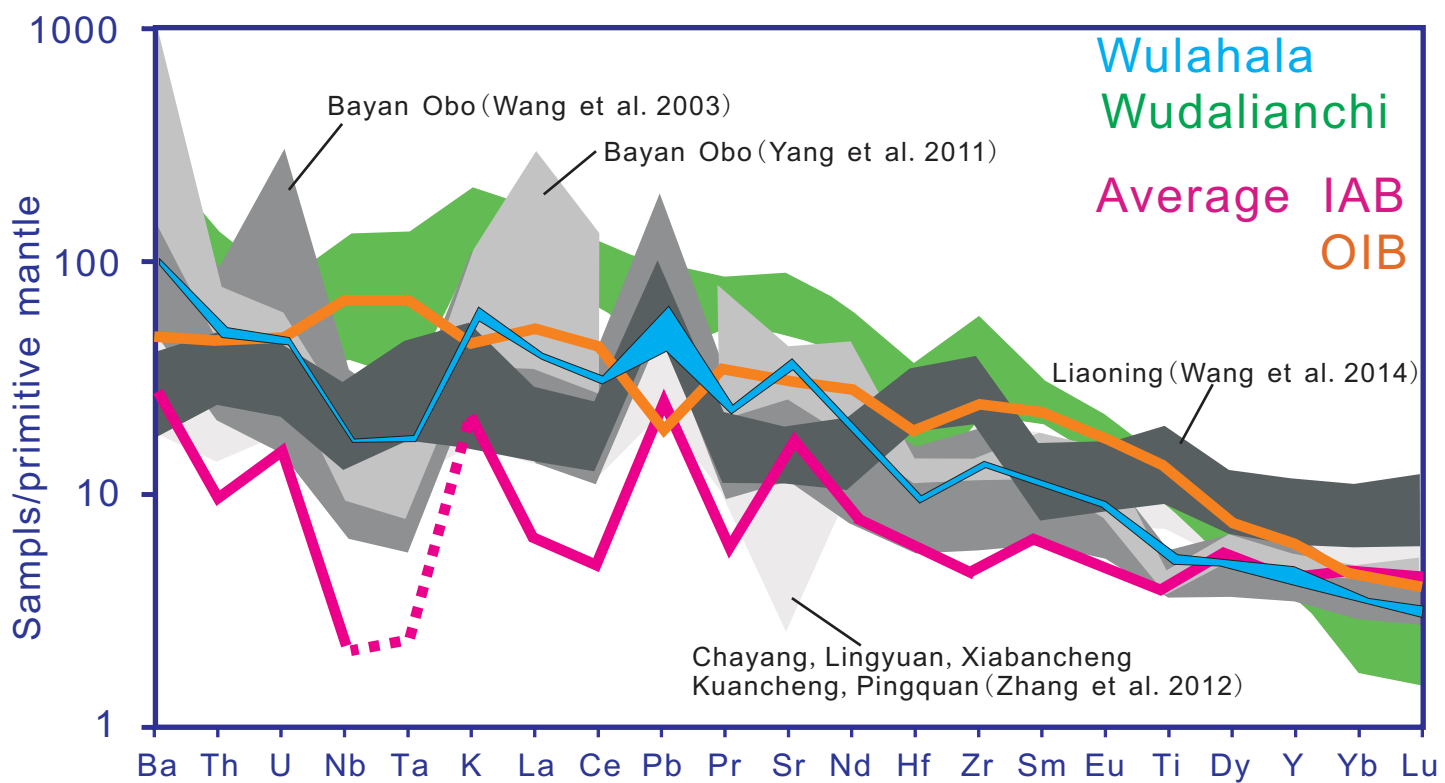


Figure DR7

Table DR1. Chemical compositions (wt.%) in Bayan Obo drill cores with different depths

| Depth(m) | TiO <sub>2</sub> | Al <sub>2</sub> O <sub>3</sub> | FeO   | MgO   | CaO   | MnO  | Na <sub>2</sub> O | K <sub>2</sub> O | P <sub>2</sub> O <sub>5</sub> | BaO  | SrO  | La <sub>2</sub> O <sub>3</sub> | Ce <sub>2</sub> O <sub>3</sub> | Pr <sub>2</sub> O <sub>3</sub> | Nd <sub>2</sub> O <sub>3</sub> | Sm <sub>2</sub> O <sub>3</sub> |
|----------|------------------|--------------------------------|-------|-------|-------|------|-------------------|------------------|-------------------------------|------|------|--------------------------------|--------------------------------|--------------------------------|--------------------------------|--------------------------------|
| 392      | 0.03             | 0.06                           | 17.20 | 13.53 | 30.91 | 4.30 | 0.08              | 0.04             | 0.04                          | 0.07 | 0.26 | 0.67                           | 1.67                           | 0.21                           | 0.68                           | 0.06                           |
| 520      | 0.06             | 0.03                           | 6.55  | 18.65 | 32.03 | 1.77 | 0.07              | 0.02             | 0.23                          | 0.44 | 0.52 | 0.36                           | 0.69                           | 0.08                           | 0.24                           | 0.02                           |
| 1048     | 0.08             | 0.98                           | 12.23 | 13.44 | 24.58 | 2.35 | 1.81              | 1.72             | 0.31                          | 0.05 | 0.63 | 0.93                           | 2.07                           | 0.20                           | 0.47                           | 0.03                           |
| 1080     | 0.05             | 1.59                           | 7.69  | 13.89 | 27.33 | 2.72 | 0.04              | 1.89             | 1.85                          | 0.20 | 0.23 | 0.59                           | 1.55                           | 0.22                           | 0.84                           | 0.09                           |
| 1336     | 0.04             | 0.14                           | 7.74  | 14.62 | 31.25 | 2.60 | 0.08              | 0.06             | 1.97                          | 0.99 | 0.31 | 0.57                           | 1.05                           | 0.12                           | 0.37                           | 0.03                           |
| 1336     | 0.04             | 0.06                           | 7.74  | 14.62 | 31.25 | 1.76 | 0.08              | 0.01             | 2.54                          | 0.15 | 0.46 | 0.56                           | 1.10                           | 0.13                           | 0.46                           | 0.05                           |
| 1402     | 0.02             | 0.07                           | 5.36  | 14.37 | 32.16 | 1.84 | 0.03              | 0.03             | 3.07                          | 0.06 | 0.19 | 1.26                           | 1.81                           | 0.17                           | 0.45                           | 0.04                           |
| 1410     | 0.02             | 0.07                           | 8.48  | 17.69 | 34.62 | 2.29 | 0.03              | 0.02             | 1.36                          | 0.04 | 0.17 | 0.67                           | 1.25                           | 0.13                           | 0.40                           | 0.04                           |
| 1461     | 0.06             | 0.06                           | 8.38  | 17.22 | 33.60 | 1.74 | 0.07              | 0.02             | 0.63                          | 0.03 | 0.81 | 1.79                           | 2.85                           | 0.28                           | 0.74                           | 0.06                           |
| 1480     | 0.05             | 0.10                           | 7.47  | 12.17 | 29.23 | 1.51 | 0.05              | 0.02             | 5.86                          | 0.13 | 0.49 | 0.75                           | 1.41                           | 0.16                           | 0.50                           | 0.06                           |
| 1502     | 0.06             | 0.09                           | 7.95  | 12.92 | 29.40 | 1.47 | 0.03              | 0.01             | 2.35                          | 0.15 | 0.47 | 1.62                           | 2.61                           | 0.27                           | 0.81                           | 0.08                           |
| 1532     | 0.03             | 0.05                           | 7.65  | 13.67 | 27.45 | 1.47 | 0.03              | 0.01             | 0.36                          | 0.59 | 0.26 | 0.33                           | 0.58                           | 0.06                           | 0.19                           | 0.02                           |
| 1574     | 0.05             | 0.04                           | 8.36  | 16.55 | 29.48 | 1.93 | 0.02              | 0.01             | 0.12                          | 1.30 | 0.35 | 1.12                           | 1.82                           | 0.19                           | 0.53                           | 0.05                           |
| 1588     | 0.36             | 0.35                           | 13.48 | 15.07 | 27.19 | 2.33 | 0.06              | 0.32             | 1.90                          | 1.86 | 0.49 | 0.65                           | 1.41                           | 0.17                           | 0.51                           | 0.05                           |
| 1612     | 0.06             | 0.09                           | 6.52  | 16.30 | 38.86 | 1.32 | 0.04              | 0.05             | 3.34                          | 0.49 | 0.39 | 2.00                           | 2.78                           | 0.27                           | 0.69                           | 0.06                           |
| 1627     | 0.25             | 0.26                           | 13.53 | 14.76 | 26.04 | 2.15 | 0.03              | 0.29             | 1.43                          | 0.22 | 0.30 | 0.93                           | 1.56                           | 0.16                           | 0.42                           | 0.04                           |
| 1641     | 0.02             | 0.08                           | 11.30 | 15.65 | 28.88 | 2.38 | 0.05              | 0.01             | 0.63                          | 0.18 | 0.16 | 0.29                           | 0.55                           | 0.06                           | 0.19                           | 0.02                           |
| 1649     | 0.05             | 0.71                           | 6.69  | 11.81 | 36.17 | 2.08 | 0.08              | 0.34             | 2.14                          | 0.24 | 0.23 | 1.08                           | 1.57                           | 0.15                           | 0.38                           | 0.04                           |
| 1676     | 0.02             | 0.07                           | 8.67  | 14.67 | 30.31 | 1.66 | 0.28              | 0.10             | 0.19                          | 0.39 | 0.57 | 1.14                           | 1.81                           | 0.17                           | 0.42                           | 0.03                           |
| 1683     | 0.06             | 0.29                           | 6.81  | 15.30 | 25.16 | 1.73 | 0.30              | 0.46             | 2.09                          | 0.53 | 0.81 | 1.67                           | 2.46                           | 0.24                           | 0.65                           | 0.05                           |
| 1692     | 0.06             | 0.21                           | 7.40  | 17.60 | 27.45 | 1.48 | 0.10              | 0.40             | 0.75                          | 0.99 | 0.83 | 0.91                           | 1.70                           | 0.17                           | 0.44                           | 0.04                           |
| 1740     | 0.04             | 0.12                           | 10.55 | 15.58 | 28.96 | 1.54 | 0.25              | 0.25             | 0.05                          | 1.10 | 0.50 | 0.52                           | 0.99                           | 0.11                           | 0.36                           | 0.03                           |
| 1765     | 0.13             | 0.08                           | 9.40  | 12.52 | 35.01 | 1.47 | 0.08              | 0.06             | 2.43                          | 0.06 | 0.25 | 1.12                           | 2.41                           | 0.26                           | 0.71                           | 0.06                           |
| 1776     | 0.03             | 0.03                           | 6.71  | 14.40 | 34.55 | 1.30 | 0.11              | 0.02             | 1.64                          | 0.62 | 0.24 | 0.91                           | 1.52                           | 0.16                           | 0.46                           | 0.04                           |

Table DR2. Monazite dating data from the drill cores in Bayan Obo

| sample | Th(ppm) | U(ppm) | Th/U   | $^{208}\text{Pb}/^{232}\text{Th}$ | $\sigma$ | Pb/Th age(Ma) | $\sigma$ |
|--------|---------|--------|--------|-----------------------------------|----------|---------------|----------|
| BO-1   | 2308    | 3.57   | 646    | 0.0462                            | 1.7      | 913           | 15       |
| BO-2   | 4197    | 1.03   | 4080   | 0.0438                            | 1.7      | 866           | 14       |
| BO-3   | 2506    | 3.04   | 825    | 0.0415                            | 1.9      | 822           | 16       |
| BO-4   | 1841    | 2.19   | 839    | 0.0410                            | 1.6      | 811           | 13       |
| BO-5   | 2138    | 2.93   | 729    | 0.0401                            | 1.6      | 795           | 13       |
| BO-6   | 2056    | 2.60   | 792    | 0.0400                            | 1.7      | 792           | 13       |
| BO-7   | 1987    | 2.32   | 858    | 0.0377                            | 1.6      | 748           | 12       |
| BO-8   | 2889    | 2.08   | 1389   | 0.0333                            | 1.8      | 662           | 12       |
| BO-9   | 1783    | 2.19   | 815    | 0.0318                            | 1.9      | 633           | 12       |
| BO-10  | 1436    | 0.97   | 1488   | 0.0288                            | 1.9      | 573           | 11       |
| BO-11  | 2294    | 2.56   | 897    | 0.0285                            | 1.6      | 569           | 9        |
| BO-12  | 1551    | 1.71   | 907    | 0.0280                            | 2.5      | 558           | 14       |
| BO-13  | 1302    | 2.55   | 511    | 0.0266                            | 1.6      | 530           | 9        |
| BO-14  | 3134    | 1.58   | 1979   | 0.0259                            | 1.6      | 517           | 8        |
| BO-15  | 4817    | 1.32   | 3643   | 0.0224                            | 2.2      | 448           | 10       |
| BO-16  | 2654    | <0.1   | >10000 | 0.0206                            | 1.6      | 413           | 7        |
| BO-17  | 2407    | <0.1   | >10000 | 0.0206                            | 1.7      | 413           | 7        |
| BO-18  | 2230    | <0.1   | >10000 | 0.0206                            | 2.0      | 411           | 8        |
| BO-19  | 2934    | <0.1   | >10000 | 0.0205                            | 1.8      | 410           | 7        |
| BO-20  | 2307    | <0.1   | >10000 | 0.0204                            | 1.8      | 408           | 8        |
| BO-21  | 1709    | 1.68   | 1015   | 0.0203                            | 1.6      | 406           | 7        |
| BO-22  | 3272    | 1.42   | 2312   | 0.0197                            | 1.8      | 394           | 7        |
| BO-23  | 1482    | 1.83   | 812    | 0.0185                            | 1.7      | 370           | 6        |
| BO-24  | 1530    | 1.30   | 1177   | 0.0180                            | 1.6      | 361           | 6        |

Table DR3. In-situ Nd isotope of monazites from Bayan Obo drill cores

| sample    | $^{147}\text{Sm}/^{144}\text{Nd}$ | $2\sigma$ | $^{143}\text{Nd}/^{144}\text{Nd}$ | $2\sigma$ | age (Ma) | $\epsilon_{\text{Nd}}(t)^{\#}$ | $T_{\text{CHUR}}(\text{Ga})$ |
|-----------|-----------------------------------|-----------|-----------------------------------|-----------|----------|--------------------------------|------------------------------|
| BO-1      | 0.04239                           | 2         | 0.511362                          | 19        | 913      | -6.9                           | 1.59                         |
| BO-2      | 0.04607                           | 5         | 0.511358                          | 32        | 866      | -8.3                           | 1.63                         |
| BO-3      | 0.04606                           | 2         | 0.511319                          | 22        | 822      | -9.9                           | 1.66                         |
| BO-4      | 0.04487                           | 4         | 0.511348                          | 23        | 811      | -9.4                           | 1.62                         |
| BO-5      | 0.04645                           | 4         | 0.511316                          | 27        | 795      | -10.5                          | 1.67                         |
| BO-6      | 0.04651                           | 5         | 0.511348                          | 22        | 792      | -10.0                          | 1.64                         |
| BO-7rim   | 0.04363                           | 8         | 0.511309                          | 37        | 748      | -11.3                          | 1.65                         |
| BO-7rim   | 0.04320                           | 4         | 0.511305                          | 39        | 748      | -11.3                          | 1.65                         |
| BO-7core  | 0.04349                           | 6         | 0.511318                          | 41        | 748      | -11.1                          | 1.64                         |
| BO-7core  | 0.04633                           | 4         | 0.511377                          | 25        | 748      | -10.2                          | 1.61                         |
| BO-8      | 0.04561                           | 7         | 0.511372                          | 22        | 662      | -11.9                          | 1.61                         |
| BO-9      | 0.04394                           | 2         | 0.511346                          | 20        | 633      | -12.9                          | 1.62                         |
| BO-10     | 0.04507                           | 14        | 0.511353                          | 25        | 573      | -14.0                          | 1.62                         |
| BO-11     | 0.04652                           | 3         | 0.511346                          | 21        | 569      | -14.3                          | 1.64                         |
| BO-12     | 0.04497                           | 4         | 0.511339                          | 19        | 558      | -14.5                          | 1.63                         |
| BO-13     | 0.04375                           | 3         | 0.511345                          | 24        | 530      | -14.9                          | 1.62                         |
| BO-14     | 0.04410                           | 10        | 0.511341                          | 34        | 517      | -15.2                          | 1.62                         |
| BO-15rim  | 0.03962                           | 8         | 0.511283                          | 38        | 448      | -17.5                          | 1.63                         |
| BO-15core | 0.04118                           | 6         | 0.511326                          | 14        | 448      | -16.7                          | 1.61                         |
| BO-16     | 0.03988                           | 3         | 0.511342                          | 26        | 413      | -17.0                          | 1.58                         |
| BO-17     | 0.03938                           | 2         | 0.511365                          | 25        | 413      | -16.5                          | 1.56                         |
| BO-18     | 0.03588                           | 9         | 0.511334                          | 27        | 411      | -17.0                          | 1.55                         |
| BO-19     | 0.04002                           | 11        | 0.511355                          | 27        | 410      | -16.8                          | 1.57                         |
| BO-20     | 0.03950                           | 4         | 0.511360                          | 23        | 408      | -16.8                          | 1.56                         |
| BO-21     | 0.04533                           | 3         | 0.511362                          | 33        | 406      | -17.1                          | 1.62                         |
| BO-22     | 0.04763                           | 20        | 0.511361                          | 24        | 394      | -17.4                          | 1.64                         |
| BO-23     | 0.04527                           | 3         | 0.511351                          | 27        | 370      | -18.0                          | 1.62                         |
| BO-24core | 0.04619                           | 7         | 0.511377                          | 22        | 361      | -17.7                          | 1.61                         |
| BO-24rim  | 0.04616                           | 2         | 0.511376                          | 23        | 361      | -17.7                          | 1.61                         |

$\epsilon_{\text{Nd}}(t)$  values are calculated based on present-day ( $^{147}\text{Sm}/^{143}\text{Nd}$ )<sub>CHUR</sub> = 0.1967 and ( $^{143}\text{Nd}/^{144}\text{Nd}$ )<sub>CHUR</sub> = 0.512638.

Table DR4. In-situ trace element compositions (ppm) of dolomite and apatite from Bayan Obo drill cores

| dolomite | primary |                  |      |      |      |      |      |      |      |      |      | recrystallization |      |      |       |      |      |      |
|----------|---------|------------------|------|------|------|------|------|------|------|------|------|-------------------|------|------|-------|------|------|------|
| Rb       | 0.05    | bdl <sup>#</sup> | bdl  | bdl  | bdl  | bdl  | bdl  | bdl  | bdl  | 0.09 | bdl  | bdl               | 0.01 | 0.01 | 0.02  | 0.01 | 0.03 | 0.04 |
| Sr       | 1766    | 1528             | 1818 | 2228 | 2174 | 2559 | 2671 | 2429 | 1197 | 2640 | 2738 | 4294              | 4513 | 4378 | 4559  | 4451 | 4289 |      |
| Ba       | 67.5    | 9.34             | 86.1 | 13.4 | 133  | 124  | 561  | 90.1 | 106  | 69.4 | 39.5 | 43.5              | 61.6 | 58.3 | 33.6  | 56.0 | 55.5 |      |
| Y        | 23.3    | 28.8             | 25   | 27.9 | 17.3 | 13.0 | 19.3 | 9.31 | 23.1 | 31.5 | 29.6 | 56.2              | 58.3 | 65.3 | 105.8 | 78.4 | 62.0 |      |
| La       | 7.18    | 3.59             | 9.17 | 4.92 | 5.25 | 5.06 | 9.63 | 3.61 | 15.5 | 65.7 | 27.4 | 36.6              | 36.6 | 56.5 | 109   | 101  | 73.8 |      |
| Ce       | 25.2    | 14.0             | 25.9 | 17.3 | 11.2 | 10.4 | 19.6 | 7.69 | 54.8 | 162  | 62.0 | 128               | 136  | 192  | 362   | 314  | 234  |      |
| Pr       | 3.83    | 2.16             | 3.65 | 2.58 | 1.39 | 1.16 | 2.36 | 0.93 | 7.50 | 15.1 | 7.50 | 17.8              | 19.6 | 26.3 | 51.8  | 43.1 | 31.4 |      |
| Nd       | 16.9    | 11.3             | 16.6 | 13.4 | 5.93 | 5.9  | 11.4 | 4.46 | 32.4 | 65.3 | 33.6 | 77.4              | 85.2 | 112  | 222   | 184  | 136  |      |
| Sm       | 5.03    | 3.37             | 4.10 | 3.94 | 1.52 | 2.67 | 4.69 | 1.81 | 6.54 | 17.1 | 8.94 | 17.9              | 20.4 | 24.8 | 47.3  | 37.0 | 28.4 |      |
| Eu       | 2.03    | 1.60             | 1.99 | 1.71 | 0.73 | 1.15 | 1.79 | 0.84 | 2.47 | 6.35 | 3.36 | 6.52              | 7.67 | 8.64 | 16.3  | 12.5 | 9.60 |      |
| Gd       | 3.99    | 3.48             | 4.12 | 3.73 | 1.75 | 2.46 | 4.45 | 2.44 | 4.79 | 14.5 | 7.22 | 15.3              | 17.5 | 19.6 | 36.8  | 28.1 | 21.7 |      |
| Tb       | 0.90    | 0.81             | 0.76 | 0.69 | 0.42 | 0.41 | 0.95 | 0.40 | 0.85 | 2.24 | 1.30 | 2.84              | 3.38 | 3.68 | 6.45  | 5.0  | 3.92 |      |
| Dy       | 5.61    | 6.23             | 5.31 | 5.16 | 2.82 | 2.86 | 4.75 | 2.26 | 5.17 | 10.3 | 6.85 | 16.2              | 18.1 | 20.1 | 33.7  | 26.1 | 20.1 |      |
| Ho       | 1.16    | 1.32             | 1.23 | 1.24 | 0.79 | 0.53 | 0.92 | 0.36 | 0.90 | 1.69 | 1.28 | 2.8               | 3.0  | 3.38 | 5.5   | 4.11 | 3.23 |      |
| Er       | 2.89    | 4.08             | 3.17 | 3.37 | 1.95 | 1.30 | 1.89 | 0.78 | 2.37 | 3.07 | 3.35 | 5.41              | 5.72 | 6.43 | 10.1  | 7.40 | 5.52 |      |
| Tm       | 0.35    | 0.61             | 0.43 | 0.38 | 0.40 | 0.17 | 0.23 | 0.10 | 0.25 | 0.32 | 0.39 | 0.55              | 0.53 | 0.58 | 0.87  | 0.64 | 0.55 |      |
| Yb       | 2.01    | 3.31             | 2.74 | 2.03 | 2.31 | 0.79 | 1.17 | 0.53 | 1.38 | 1.39 | 2.0  | 2.18              | 2.18 | 2.50 | 3.75  | 2.90 | 2.24 |      |
| Lu       | 0.20    | 0.39             | 0.22 | 0.17 | 0.29 | 0.11 | 0.14 | 0.04 | 0.17 | 0.12 | 0.22 | 0.18              | 0.20 | 0.23 | 0.32  | 0.21 | 0.21 |      |

Table DR4. continued

| apatite | primary |      |      |      |      |      |      |      |      |      |      | recrystallization |      |  |  |  |  |
|---------|---------|------|------|------|------|------|------|------|------|------|------|-------------------|------|--|--|--|--|
| Rb      | 0.14    | 1.40 | 0.26 | 0.26 | 3.01 | 0.10 | 0.08 | 0.04 | 0.12 | 0.14 | 0.12 | 0.48              | 0.18 |  |  |  |  |
| Sr      | 5109    | 4026 | 5006 | 4586 | 3982 | 2834 | 2663 | 2956 | 2942 | 2364 | 3257 | 3255              | 3223 |  |  |  |  |
| Ba      | 22.9    | 22.7 | 62.4 | 35.3 | 17   | 83   | 94   | 133  | 204  | 78.2 | 64.3 | 66.7              | 223  |  |  |  |  |
| Y       | 1356    | 1153 | 1246 | 1193 | 1107 | 128  | 102  | 121  | 116  | 144  | 183  | 212               | 119  |  |  |  |  |

|    |      |      |      |      |      |      |      |      |      |      |      |      |      |
|----|------|------|------|------|------|------|------|------|------|------|------|------|------|
| La | 2133 | 1598 | 1918 | 1553 | 1412 | 158  | 157  | 202  | 241  | 564  | 495  | 846  | 339  |
| Ce | 7601 | 5809 | 6852 | 5646 | 6075 | 585  | 525  | 684  | 779  | 1505 | 1387 | 2372 | 1114 |
| Pr | 1188 | 937  | 1035 | 912  | 1004 | 96.7 | 82   | 104  | 109  | 228  | 187  | 335  | 146  |
| Nd | 5830 | 4406 | 4954 | 4553 | 5151 | 500  | 405  | 516  | 517  | 982  | 827  | 1394 | 647  |
| Sm | 1227 | 902  | 1051 | 947  | 1059 | 106  | 88.4 | 103  | 100  | 161  | 144  | 208  | 116  |
| Eu | 338  | 251  | 287  | 265  | 278  | 26.0 | 21.3 | 25.5 | 24.8 | 37.2 | 35.9 | 49.2 | 27.1 |
| Gd | 800  | 620  | 714  | 675  | 680  | 61.6 | 52.8 | 61.7 | 60.6 | 89.5 | 85.2 | 116  | 67.8 |
| Tb | 102  | 76.6 | 90.0 | 83.5 | 78.7 | 6.75 | 5.6  | 6.55 | 6.05 | 8.35 | 9.24 | 11.5 | 7.06 |
| Dy | 497  | 376  | 451  | 417  | 377  | 36.3 | 29.3 | 34.2 | 31.9 | 40.9 | 49.4 | 58.2 | 33.5 |
| Ho | 72.3 | 54.7 | 65.9 | 61.6 | 53.6 | 5.79 | 4.68 | 5.85 | 5.38 | 6.51 | 8.17 | 9.48 | 5.47 |
| Er | 132  | 102  | 124  | 118  | 99.9 | 13.8 | 10.7 | 12.8 | 12.4 | 14.7 | 19.0 | 22.5 | 12.1 |
| Tm | 11.1 | 8.50 | 10.3 | 9.92 | 8.02 | 1.45 | 1.07 | 1.37 | 1.42 | 1.53 | 1.94 | 2.19 | 1.21 |
| Yb | 38.9 | 30.3 | 37.1 | 36.8 | 28.9 | 6.76 | 5.25 | 6.1  | 6.95 | 7.24 | 8.45 | 10.3 | 5.89 |
| Lu | 3.07 | 2.40 | 2.98 | 3.03 | 2.35 | 0.63 | 0.50 | 0.61 | 0.79 | 0.70 | 0.78 | 0.99 | 0.58 |

---

#below determination limits.

Table DR5. In-situ Sr isotope of dolomite and apatite from Bayan Obo drill cores

| dolomite                        |           |                                 |           | apatite                         |           |                                 |           |
|---------------------------------|-----------|---------------------------------|-----------|---------------------------------|-----------|---------------------------------|-----------|
| primary                         |           | recrystallization               |           | primary                         |           | recrystallization               |           |
| $^{87}\text{Sr}/^{86}\text{Sr}$ | $2\sigma$ | $^{87}\text{Sr}/^{86}\text{Sr}$ | $2\sigma$ | $^{87}\text{Sr}/^{86}\text{Sr}$ | $2\sigma$ | $^{87}\text{Sr}/^{86}\text{Sr}$ | $2\sigma$ |
| 0.70250                         | 25        | 0.70606                         | 33        | 0.70296                         | 19        | 0.70351                         | 8         |
| 0.70241                         | 20        | 0.70669                         | 67        | 0.70294                         | 17        | 0.70323                         | 19        |
| 0.70238                         | 22        | 0.70384                         | 22        | 0.70293                         | 23        | 0.70345                         | 13        |
| 0.70271                         | 12        | 0.70946                         | 53        | 0.70297                         | 19        | 0.70349                         | 7         |
| 0.70293                         | 16        | 0.70760                         | 81        | 0.70297                         | 34        | 0.70357                         | 16        |
| 0.70287                         | 9         | 0.70456                         | 35        |                                 |           | 0.70357                         | 18        |
| 0.70290                         | 14        | 0.70786                         | 50        |                                 |           | 0.70367                         | 11        |
| 0.70280                         | 9         | 0.70682                         | 21        |                                 |           | 0.70347                         | 14        |
| 0.70297                         | 10        | 0.70572                         | 10        |                                 |           | 0.70347                         | 12        |
| 0.70284                         | 14        | 0.70971                         | 19        |                                 |           | 0.70364                         | 18        |
| 0.70290                         | 9         | 0.70889                         | 10        |                                 |           | 0.70341                         | 13        |
| 0.70289                         | 4         | 0.70871                         | 17        |                                 |           | 0.70354                         | 13        |
| 0.70281                         | 9         | 0.70533                         | 14        |                                 |           |                                 |           |
| 0.70282                         | 5         | 0.70568                         | 23        |                                 |           |                                 |           |
| 0.70295                         | 8         | 0.70827                         | 26        |                                 |           |                                 |           |
| 0.70294                         | 3         | 0.70718                         | 35        |                                 |           |                                 |           |
| 0.70285                         | 7         | 0.70467                         | 11        |                                 |           |                                 |           |
| 0.70279                         | 4         |                                 |           |                                 |           |                                 |           |